This is an Accepted Manuscript version of the following article, accepted for publication in:

Thrust Ripple Reduction in Linear Switched-Flux Machines via Additional Pole Optimisation

Imanol Eguren, Gaizka Almandoz, *Member, IEEE,* Aritz Egea, Sergio Zarate, and Ander Urdangarin

Abstract—Linear switched-flux machines are a kind of permanent magnet machine with a passive ferromagnetic secondary. Therefore, they can achieve both a good performance and a low cost in long stroke applications. However, due to the end effect, these machines generate high detent force and on load thrust force ripples. There are several solutions in the literature that aim to minimise the thrust ripple. One of those solutions is the placement of additional poles in the ends of the machine. These can be passive, *i. e.* simple ferromagnetic teeth, or active, with additional magnets. The former is the most common solution in the literature. In this article, the optimal configuration of the additional poles is discussed via 4 additional pole sizing strategies, and the influence of the design variables and optimisation objectives is analysed. Then, a generic additional pole configuration is proposed, which combines a high effectiveness and a simple design. Finally, an experimental validation is carried out, and the measurements confirm the results from the optimisation.

Index Terms—End effect, Linear machines, Optimisation, Ripple, Switched-Flux, Magnet.

I. INTRODUCTION

THESE last years, the industry is looking for highly efficient, cost effective and tightly integrated devices, no matter the application. Electrical machines are not an exception. Rotating machines are commonly used to generate linear motion. In the beginning, they were combined with mechanical gears to obtain the desired travelling speed. Then, gearless direct-drive machines were able to remove the mechanical gear, offering more compact and reliable drives. Linear machines are a particular configuration of direct-drive machine that can exert linear thrust force without any sheaves, gears, or contact between the primary and secondary sides [1], [2]. This feature allows linear machines a highly precise operation [3], [4], with low noise [5], [6] and high reliability [7], [8].

However, the abrupt change of the magnetic circuit in the ends of linear machines generates a flux leakage in the end poles. In the particular case of linear switched-flux permanent magnet machines (LSFPMs), they suffer from a heavy saturation [9], which increases the severity of this phenomenon. In 3 phase machines, this translates to an unbalance between
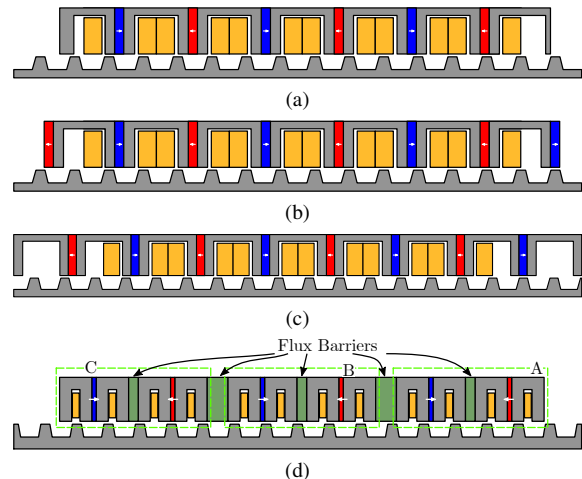
Fig. 1: LSFPMs with thrust ripple minimising configurations. (a) Passive additional poles, (b) active additional poles, (c) multiple additional poles and (d) modular and complementary structure.

the magnetic circuit that is perceived by the different phases of the machine.

This phenomenon influences the thrust ripple in 3 major ways. First, the flux leakage creates a ripple component of the no load thrust force [10]. Then, even if the back-EMF is sinusoidal in LSFPMs, its unbalance creates harmonic components when converted to the dq frame. These harmonics create an additional component of the thrust fluctuation when the machines are fed with sinusoidal currents [5]. Finally, due to the structure of linear machines, the unbalance also exists between the different phase inductances. This creates an additional ripple component that is proportional to the squared value of the supply current [11].

When talking about linear synchronous machines, the most common solution for the minimisation of the detent force is the modification of the geometry of the ends of the mover to compensate the fluctuations of the force [12], [13]. The most frequent modification is the addition of an extra ferromagnetic tooth at each of the ends of the machines [14], [15]. The configuration is shown in figure 1 (a). These teeth move the ends of the machine to the point to where the amplitude of the detent force is minimised.

If additional PMs are placed in these extra teeth like in figure 1 (b), the back-EMF unbalance can also be compensated [5], [8]. When adopting this configuration, the publications from the literature select the balancing of the fundamental phase back-EMF amplitudes as the optimisation objective [8], [16]. However, this back-EMF balancing strategy often ends up with configurations that increase the peak to peak detent

force [8], [16].

Hence, alternative configurations have also been presented, where multiple additional teeth are placed at each of the sides of the machine [17]. The idea behind this configuration is to compensate the back-EMF unbalance with the additional PMs, and to minimise the detent force amplitude with the passive assistant teeth. This configuration is shown in figure 1 (c).

None of the first three structures from figure 1 are able to suppress the phase inductance unbalance. In order to obtain this balancing effect, all the phases must observe the same magnetic circuit. Therefore, the solution for the inductance unbalance is to use a modular structure [11]. There are different alternatives to modularise the machines [18]. However, the idea behind most of them is quite similar. Figure 1 (d) shows a possible configuration of a LSFPM with a modular structure. In these machines, each of the individual modules are separated by a non magnetic flux barrier. The flux barriers decouple the modules, and consequently, the mutual inductances are almost entirely suppressed. As the magnetic circuit that each of the modules observes is almost the same, the self inductances are also balanced. Hence, the overall phase inductances are also balanced. Additionally, as the modules are essentially symmetrical between them, all the phases generate the same back-EMF. Consequently, it can be stated that the modular configuration is the best possibility when a completely balanced machine is desired.

Moreover, the modules of the individual phases must be displaced $\frac{1}{3}$ of a secondary pitch between each other. Due to this displacement, some of the harmonics of the detent force and the thrust ripple are compensated between the different modules. Furthermore, if the modular structure is combined with a complementary magnetic circuit like in figure 1 (d), the odd order harmonics of the detent force and the even harmonics of the back-EMF are also suppressed [19].

However, the mechanical structure of modular and complementary machines is quite complex, which could impact their manufacturing cost. Besides this, the balancing effect of the magnetic circuit is obtained because the end effect actually exists in every single one of the modules that are used in the machine.

The average value of the Carter coefficient, K_c, to account for the increase in the airgap length in a single-module 6/13 machine due to the end-effect can be approximated with

$$K_c = \frac{6}{5 + \frac{1}{1 + \frac{4g}{\pi \tau_p} \ln\left(1 + \frac{\pi \omega_e}{2g}\right)}}, \tag{1}$$

where g is the airgap length, τ_p is the primary pitch, and ω_e is the width of the ends of the machine, whose can be approximated to be equal to the height of the primary of the machine.

Notice in (1) that if $\omega_e > 0$, the expression results in a value that is greater than 1. This means that the more present the end-effect is, the larger the force loss will be in the machine.

Consequently, the thrust density of the modular machines is reduced significantly, due to the larger amount of ends than a single-module machine. This, together with the additional length that is required for the installation of the flux barriers,
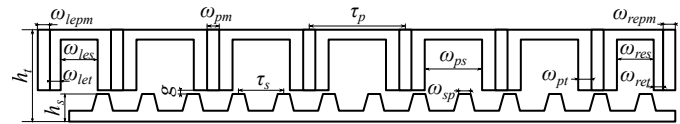

Fig. 2: Geometric parameters of the machine.

increases the bulk of modular machines. Hence, it is the passive ferromagnetic assistant teeth which are most commonly used in the literature to deal with the thrust ripple. However, the performance of the passive ferromagnetic teeth can be improved if they are complemented with additional PMs.

Summarising, on the one hand it can be concluded that the simple single-module configurations that can be found in the literature are not very effective when minimising the thrust fluctiations. On the other hand, the modular configurations are demonstrated to be highly effective, but they are quite complex to be built and they reduce the thrust density of the machines. In this article, two highly effective design solutions are presented to minimise the detent force and the thrust ripple of LSFPMs, which do not compromise their thrust capability and compactness. The effectiveness of one of the proposed configurations is experimentally validated, obtaining a good agreement between the simulation results and the experimental measurements. In order to explore the rate of improvement with the new configuration, the solutions that were previously proposed in the literature are also prototyped, and the results demonstrate the superior performance of the proposed configuration.

In the presented work, the optimal configuration of the additional poles is discussed via 4 different additional pole sizing strategies. The influence of the selection of design variables and the optimisation objectives is studied, and the best possibility is identified. In this way, a generic configuration of a single-module LSFPM is proposed. This generic configuration allows an easy sizing and a close to minimal thrust ripple for single module machines. The article is the continuation of the work that was presented in [20].

The article is organised as follows: the performance of the original machine with no extra poles is analysed in section II. Section III describes the 2D and 3D FEM models that were used to analyse the thrust ripples of the different machines. Section IV explains the different machine configurations and their optimisation strategy. The experimental validation of the results is given in section V, and section VI gathers the conclusions of this study.

II. ANALYSIS OF THE ORIGINAL THRUST RIPPLE

The machine that is analysed in this paper is the 6 primary pole and 13 secondary pole C-Core linear switched-flux machine. The main geometric parameters of the machine are given in table I and described in figure 2. The values of the parameters of the machine were defined following the optimisation results from [14].

The two main components of the detent force, *viz.*, the end effect force and the slot effect force, can be decomposed via a simple procedure. First, a virtual periodic machine with an infinite length must be simulated. As this machine has no ends,

TABLE I: Main parameters of the simulation models.

| Parameter	Symbol	Unit	Value
Total Height	h_t	mm	21
Stack Length	l_{stk}	mm	30
Airgap	g	mm	1
Secondary Height	h_s	mm	5.6
Secondary Pole Pitch	τ_s	mm	144/13
Secondary Pole Width	ω_{sp}	mm	3.1
Primary Pitch	τ_p	mm	24
PM Width	ω_{pm}	mm	3
Primary Tooth Width	ω_{pt}	mm	4.1
Primary Slot Width	ω_{ps}	mm	12.8
Rated Speed	V	m/s	1
Rated Current	I	A	1.44
Phase Turns	N_{ph}	Turns	234
Fill Factor	K_f	-	0.45
PM material	-	-	N35H
Lamination Material	-	-	M800-65A
PM Remanence	B_r	T	1.17
PM Relative Permeability	μ_r	-	1.01
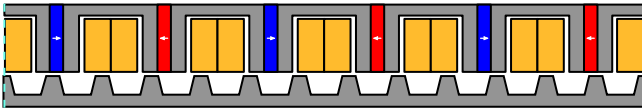
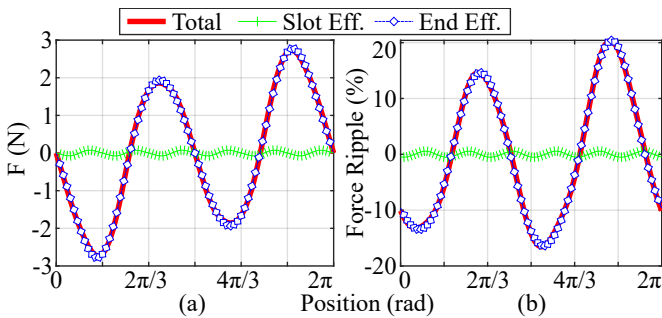Fig. 3: Periodic model for the computation of the slot-effect.

Fig. 4: Decomposition of the components of the thrust ripple. (a) Open circuit simulation, and (b) rated load.

the end effect will not be present. Therefore, the only ripple is the one that is caused by the primary slots. Figure 3 shows an example of a virtual periodic machine.

Then, the real machine is simulated, and the end effect force F_e is obtained by subtracting the slot effect force F_s to the total detent force, F_d,

$$F_e = F_d - F_s. \qquad (2)$$

The same procedure can also be applied in a simulation where the machine is fed with sinusoidal currents. In this way, the influence of the end effect over the on load thrust ripple can be obtained.

The result from the decomposition of the thrust ripple components is given in figure 4. The original peak to peak detent force amplitude is 5.49 N, and the original thrust ripple is 36.9 %.

The dominant component of the thrust ripple in the analysed machine is the end effect. Notice in figure 4 that the total force is almost entirely generated by the end effect component. In figure 5, it can be seen that the second order harmonic is clearly the dominant component of the ripple. Therefore, the
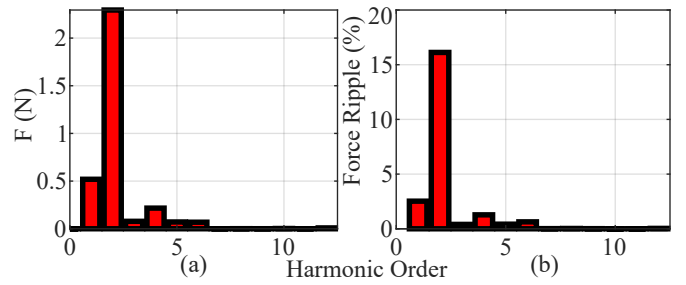

Fig. 5: Spectra of the thrust fluctuations of the initial machine. (a) Open circuit (b) rated load.

TABLE II: Initial state of the unbalanced parameters.

Parameter	Symbol	Unit	Value
Electromotive force, phase a	E_a	V (peak)	6.75
Electromotive force, phase b	E_b	V (peak)	8.26
Electromotive force, phase c	E_c	V (peak)	6.75
Self inductance, phase a	L_{aa}	mH	4.65
Self inductance, phase b	L_{bb}	mH	5.31
Self inductance, phase c	L_{cc}	mH	4.65
Mutual inductance, phases ab	$M_{ab} = M_{ba}$	mH	-2.41
Mutual inductance, phases ac	$M_{ac} = M_{ca}$	mH	-1.64
Mutual inductance, phases bc	$M_{bc} = M_{cb}$	mH	-2.41

usage of a complementary magnetic circuit would not be very effective for this machine.

As for the unbalance in the electrical parameters, table II shows the phase back-EMF and inductance values. In the initial configuration, the unbalance is quite significant in all of the parameters.

III. DESCRIPTION OF THE FEM MODELS

All the simulations of the study were performed in Altair® Flux®. Figure 6 shows the 2D and 3D models of the configuration with active additional poles. Although the active part of the machine is constituted by 6 primary poles and 13 secondary teeth, the total length of all the simulation models of the study was defined as $27\tau_s$. The extra length was introduced for allowing the flux to escape from the edges of the machine, creating the end-effect. A clearance of 14.5 mm was also left at the top of the machine, to allow the presence of the PM flux leakage.

In the case of the 3D models, an axial clearance of 14.5 mm was also left to accommodate the end-windings, and to account for the transverse end-effect.

In order to ensure a high precision of the simulations, a second order mesh was used in the models. Additionally, the exact same airgap mesh was used in all the 2D and 3D models. It consisted of 3 layers, with the centre layer consisting of rectangular elements. The mesh of the airgap region can be observed in detail in figure 7. The length of the mesh elements was set as $\tau_s/72$, so that there were 72 mesh elements per secondary pole pitch. The thrust force was computed with 73 samples over a secondary pole pitch in the 2D simulations, and with 25 samples in the 3D simulations. The electrical position of the first and last samples of the simulations is the same, hence, the mover of the machine was displaced 1 mesh element in the 2D simulations, and 3 mesh elements in the 3D
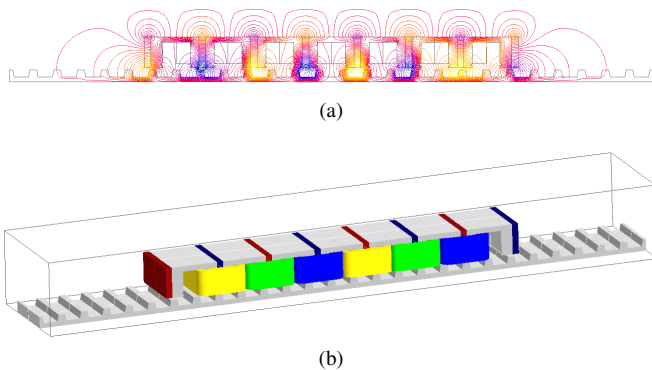
Fig. 6: (a) 2D and (b) 3D FEM models of the machine with active additional poles.
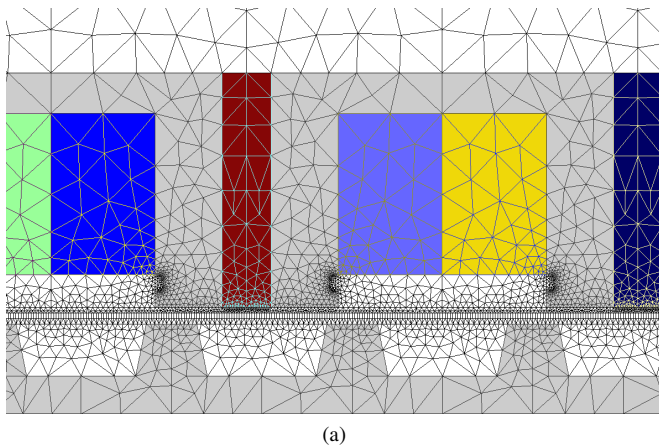

Fig. 7: Detail of the airgap mesh of the model.

simulations. The virtual work method was used to compute the forces in each of the time steps of the simulations,

$$\vec{F} = \frac{\partial W_m}{\partial l}. \tag{3}$$

IV. OPTIMISATION OF THE THRUST RIPPLE

A. Passive Ferromagnetic Poles

The passive ferromagnetic poles or assistant teeth are commonly optimised via an individual parameter optimisation [14], [21]. In this process either the position of the assistant teeth or the position of the teeth plus their width are individually swept, looking for the point where the amplitude of the peak to peak detent force is the lowest. However, in this article, in order to explore the limits of the performance of the passive ferromagnetic poles, their widths, ω_{let} and ω_{ret} for left and right respectively and position ω_{les} and ω_{res}, are globally optimised with the nondominated sorting genetic algorithm (NSGA-II) [22], and the minimisation of both the peak to peak detent force and the on load thrust ripple are set as the optimisation objectives. Hence, the peak to peak value of the detent force is obtained first from a no load simulation, and the machine is then simulated at rated load to obtain the on load thrust ripple. The configuration parameters of the optimisation are given in table III.

TABLE III: Configuration of the GA for the optimisation of the assistant teeth.

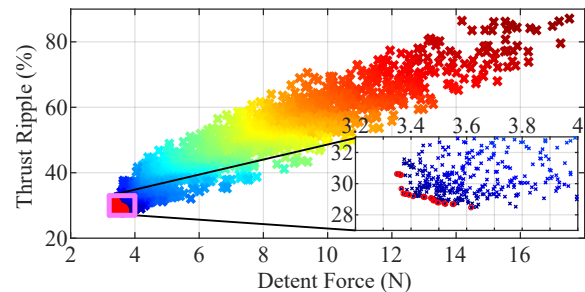| Parameter	Value/Range	Resolution
ω_{let} & ω_{ret}	0.1 mm $\leftrightarrow 2\omega_{pt}$	0.05
ω_{les} & ω_{res}	$\omega_{ps}/2 \leftrightarrow 2\omega_{ps}$	0.05
Population Size	100	
Number of Parents	20	
Mutation Rate	0.05	

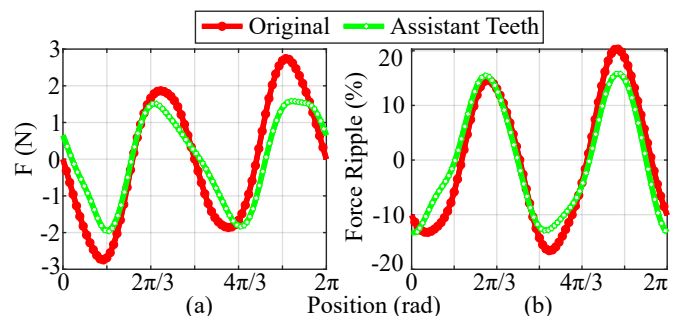Fig. 8: Result from the optimisation of the assistant teeth.

Fig. 9: Waveforms of the thrust fluctuations of the machine with optimised assistant teeth. (a) Open circuit (b) rated load.

Figure 8 shows the values of the detent force and thrust force ripple of the candidates that were analysed by the GA. The optimal nondominated candidates are marked with a red circle. It can clearly be seen in figure 8 that the assistant teeth solution is quite effective when dealing with the open-circuit thrust ripple. However, the on load ripple is not reduced as much as the detent force is. Figure 9 shows the waveforms of the machine with the optimised ends, and figure 10 shows the spectra of its thrust fluctuations. Notice that the influence of the passive additional poles is quite limited for the 2nd order harmonic.

B. Active Additional Poles - Balancing the Phase Back-EMF

It can be argued that the popularity of the passive assistant teeth solution is brought by its ease of design. The high simplicity and easy manufacturing make them very attractive. The generic active poles should therefore match or at least get close to the convenience of that solution. A simple design process is the first requirement. Hence, in this section, the capabilities of the design procedure that is most commonly found in the literature are analysed.

In this first alternative, the widths of the additional magnets, ω_{lepm} and ω_{repm}, are varied until the fundamental open circuit
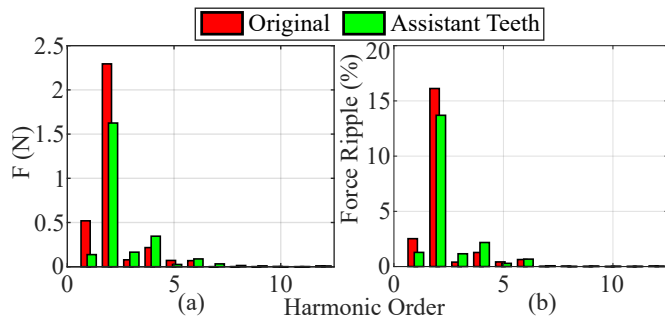
Fig. 10: Spectra of the thrust fluctuations of the machine with optimised assistant teeth. (a) Open circuit (b) rated load.
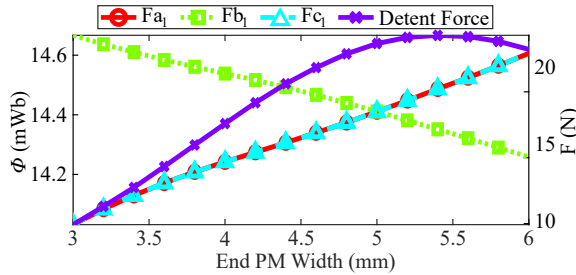

Fig. 11: Result of the optimisation of the active additional poles for balancing the fundamental flux linkage.
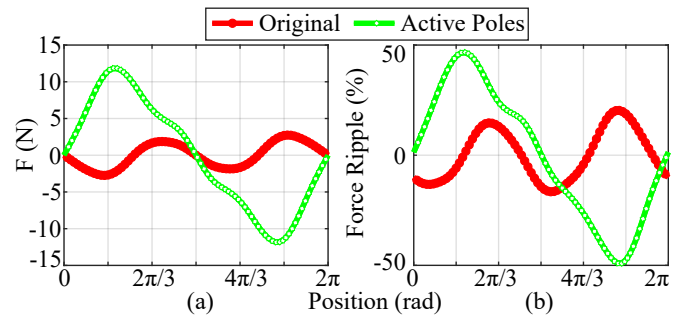

Fig. 12: Waveforms of the thrust fluctuations of the machine when the active additional poles are optimised for a minimised back-EMF unbalance. (a) Open circuit (b) rated load.
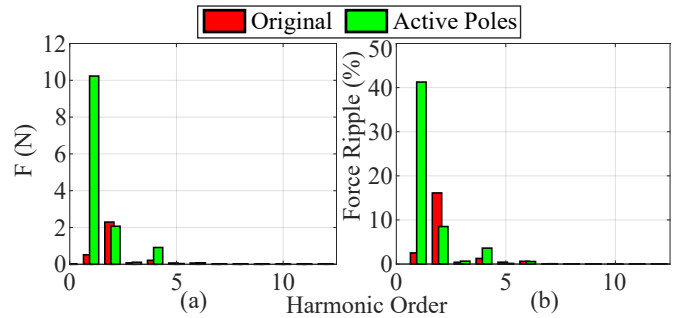

Fig. 13: Spectra of the thrust fluctuations of the machine when the active additional poles are optimised for a minimised back-EMF unbalance. (a) Open circuit (b) rated load.

flux linkage values are completely balanced. The width of both additional magnets is kept equal during the sizing process. Therefore, it is a single variable and single objective scenario, and the genetic algorithm is not necessary. It has been found in the literature review that this solution can increase the value of the peak to peak detent force ripple. Thus, its amplitude is also monitored during the sizing of the end poles.

The result of the optimisation procedure is given in figure 11. Notice how as the flux linkages balance, the trend of the detent force is to increase its amplitude. Hence, it can be concluded that this solution is not an effective way to minimise its value. In fact, the amplitude of the detent force ripple, with 23.66 N, is 430.97 % of that of the initial machine. The amplitude of the detent force is so high, that even the thrust ripple at rated current increases, going from the 36.9 % ripple of the initial machine to a 95.65 %.

The waveforms of the machine are now given in figure 12, and the spectra in figure 13. Interestingly, the dominant harmonic of the thrust ripple is switched, and now it's the first harmonic which fluctuates the most. This is why the combination of this solution with a complementary magnetic circuit is an effective way to minimise the thrust ripple. This configuration is explained in more detail in [5]. However, the combination with a complementary magnetic circuit requires the usage of more than a single machine module. Thus, it increases the complexity and the manufacturing cost of the machine.

C. Active Additional Poles - Minimising the Detent Force

Notice that the unbalance between the phase flux linkages is already quite low in figure 11 when the width of the additional

magnets is of 3 mm. Knowing that this is the same width as the one of the rest of the magnets of the machine, a better strategy when sizing the additional poles can be defined. In this second alternative, the PMs of the additional poles are the same as those of the active part of the machine, and the additional poles are placed at the point where the amplitude of the detent force is minimised. In this way, the balancing effect over the flux linkages is obtained thanks to the placement of the additional magnets, and a reduction of the peak to peak detent force is ensured. Hence, in this case, the widths of the end teeth, ω_{let} and ω_{ret}, are the optimisation variables.

The optimisation problem is still quite simple for this configuration. Therefore, the usage of a genetic algorithm is not strictly necessary. Here, the optimisation is done via a grid search. The results of the optimisation are given in figure 14.

The effectiveness of this approach is much higher than the one of the previous configurations for both the detent force and the thrust ripple. The optimised waveforms are given in figure 15 and the spectra in figure 16. The amplitude of the second order harmonic is reduced significantly, whilst the previous configurations were unable to deal with this harmonic. Hence, a very significant reduction is obtained in the amplitude of both ripples, with a final value of 2.16 N for the detent force and a 11.35 % for the force ripple at rated load.
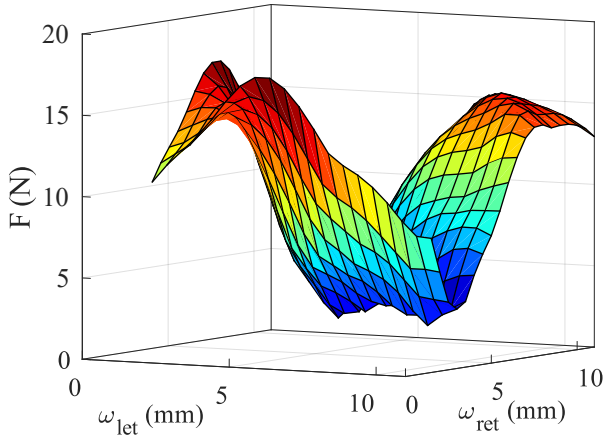
Fig. 14: Result of the optimisation of the active additional poles for minimising the detent force.
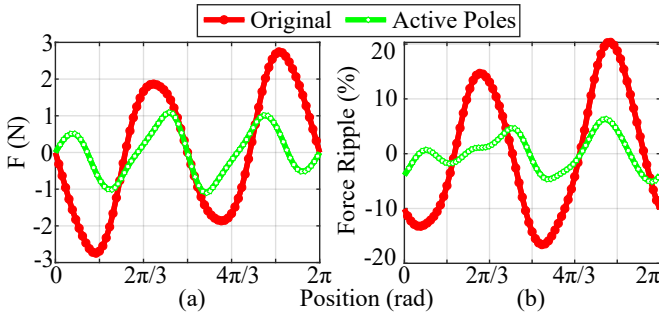

Fig. 15: Waveforms of the thrust fluctuations of the machine when the active additional poles are optimised for a minimised detent force. (a) Open circuit (b) rated load.
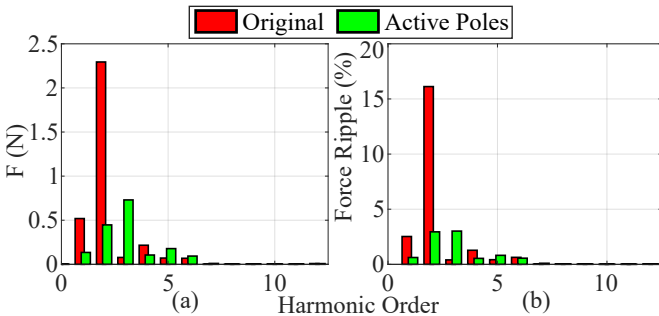

Fig. 16: Spectra of the thrust fluctuations of the machine when the active additional poles are optimised for a minimised detent force. (a) Open circuit (b) rated load.

D. Active Additional Poles - Global Optimisation

With the aim of exploring the limits of the capability of the active end poles when dealing with the thrust ripples, the widths of the end teeth, ω_{let} and ω_{ret}, and the widths of the end PMs, ω_{lepm} and ω_{repm}, are optimised in this section with the genetic algorithm to minimise both the detent force amplitude and the rated thrust ripple. A summary of the optimisation is given in table IV.

The global optimisation of the active additional poles is by far the most effective way for a minimised detent force
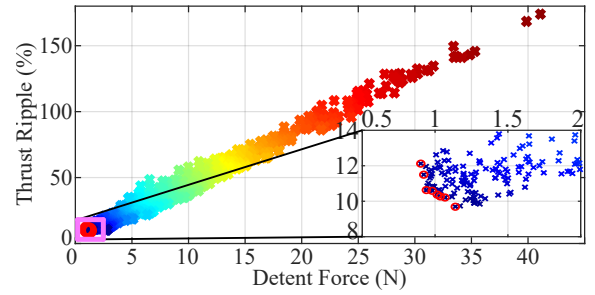

Fig. 17: Result of the global optimisation of the active additional poles.

TABLE IV: Configuration of the GA for the global optimisation of the active additional poles.

Parameter	Value/Range	Resolution
ω_{let} & ω_{ret}	0.1 mm $\leftrightarrow$ $2\omega_{pt}$	0.05
ω_{lepm} & ω_{repm}	0.1 mm $\leftrightarrow$ $2\omega_{pm}$	0.1
Population Size	100	
Number of Parents	20	
Mutation Rate	0.05	

Fig. 18: Waveforms of the thrust fluctuations of the machine when the active additional poles are globally optimised. (a) Open circuit (b) rated load.

amplitude. Figure 17 shows the results of the global optimisation. The figure shows the detent force and the thrust ripple result of all the design candidates that were analysed by the genetic algorithm, and the nondominated solutions are highlighted again with red circles. If this result is compared to that from figure 8, and knowing that the difference between the two configurations lays in the addition of the end PMs, it can be clearly stated that the attachment of those extra magnets is a very effective way to minimise the thrust fluctuations in linear switched-flux machines.

However, the reduction of the on load thrust ripple is almost on pair with that of the previous configuration. The waveforms in figure 18 and figure 19 also show that the effectiveness of this alternative is also very high on both the no load and the on load thrust ripple.

E. Comparison of results

A summary of the optimisation approaches and their respective results can be found in table V. The self and mutual inductances of the different machine configurations were calculated with the frozen permeability method. Notice that as it

This article has been accepted for publication in IEEE Transactions on Energy Conversion. This is the author's version which has not been fully edited and content may change prior to final publication. Citation information: DOI 10.1109/TEC.2022.3160505

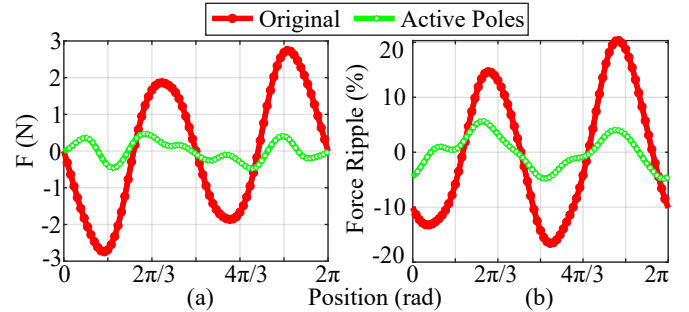IEEE TRANSACTIONS ON ENERGY CONVERSION, VOL. XX, NO. X, MONTH 20XX 7
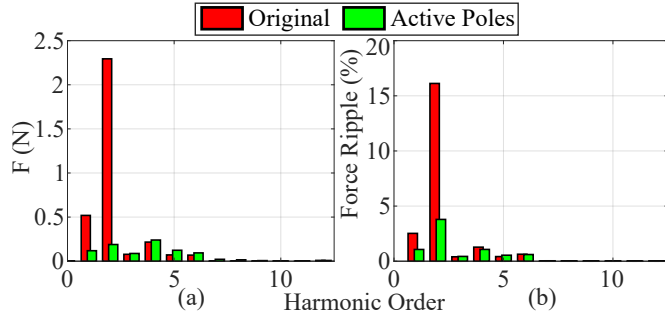
Fig. 19: Spectra of the thrust fluctuations of the machine when the active additional poles are globally optimised. (a) Open circuit (b) rated load.

TABLE V: Comparison of optimisation approaches. The optimisation variables are denoted with an asterisk (*).

Parameter	Initial	Passive Poles	Active Poles		
Objective	-	$F_d \downarrow, F_r \downarrow$	$E_a = E_b = E_c$	$F_d \downarrow$	$F_d \downarrow$ and $F_r \downarrow$
Method	-	GA	Grid search	Grid search	GA
ω_{let} (mm)	-	1.85*	4.1	5.5*	4.8*
ω_{ret} (mm)	-	4.55*	4.1	5.5*	4.55*
ω_{les} (mm)	6.4	12.4*	12.8	12.8	12.8
ω_{res} (mm)	6.4	10.55*	12.8	12.8	12.8
ω_{lepm} (mm)	-	-	5*	3	2.2*
ω_{repm} (mm)	-	-	5*	3	1.9*
F_d (N)	5.49	3.53	23.66	2.16	0.94
F_r (%)	36.9	29.09	95.65	11.35	10.38
E_a (V peak)	6.75	7.03	8.18	7.51	7.42
E_b (V peak)	8.26	8.59	8.18	8.52	8.57
E_c (V peak)	6.75	7.03	8.18	7.51	7.44
L_{aa} (mH)	4.65	5.23	5.34	5.40	5.37
L_{bb} (mH)	5.31	5.41	5.47	5.47	5.46
L_{cc} (mH)	4.65	5.36	5.34	5.40	5.36
M_{ab} (mH)	-2.41	-2.27	-2.23	-2.22	-2.23
M_{bc} (mH)	-2.41	-2.24	-2.23	-2.22	-2.23
M_{ca} (mH)	-1.64	-1.54	-1.53	-1.52	-1.53

(a)

(b)

Fig. 20: q-frame back-EMF (a) waveform and (b) spectra.

was expected, none of the configurations is able to suppress the unbalance between the mutual inductances. However, all the configurations, including the passive poles, are able to reduce the unbalance between the self inductances.

Figure 20 provides the waveforms and the spectra of the q-frame back-EMF of the different configurations. Notice that the 2 machines without active poles present a much more noticeable ripple in the q-frame. The spectra in figure 20 (b) shows that both these machines have to deal with a non-neglectable second order harmonic in the q-frame back-EMF. This component originates from the unbalance of the fundamental component of the phase back-EMF amplitudes. This is why all the machines with active poles are able to minimise the amplitude of this second order harmonic, which results in a reduced on-load thrust ripple.

V. VALIDATION OF RESULTS

In order to validate the results from this analysis, the initial machine, the machine with passive ferromagnetic poles (C1), the machine with the back-EMF balancing strategy (C2), and the machine with active additional teeth which were sized for a minimised detent force (C3), were prototyped. Due to budget limitations, the prototypes were manufactured in solid carbon steel, F-1110 for the primary and F-1140 for the secondary, instead of the M800-65A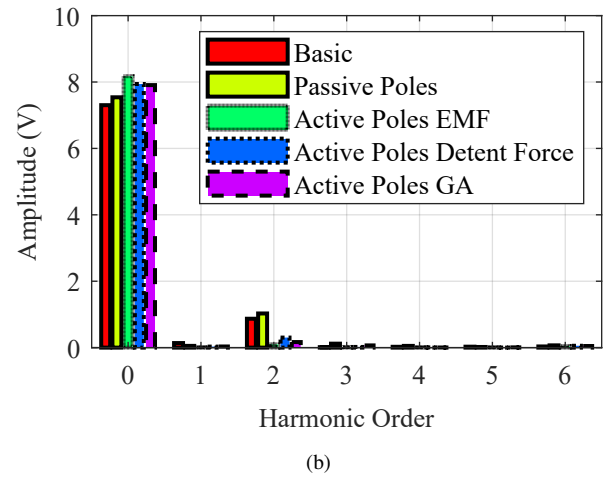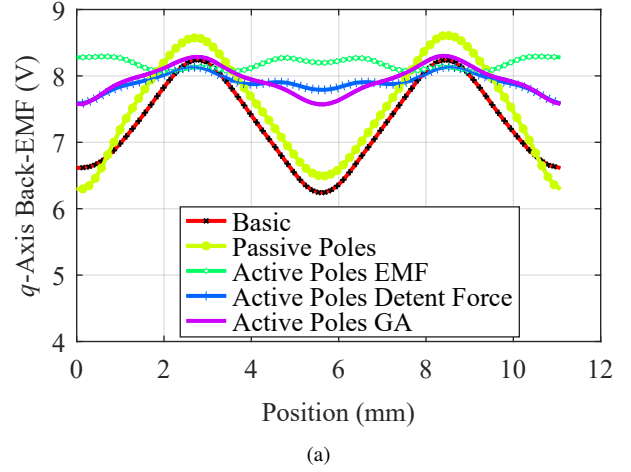 silicon steel that they were initially optimised for. The BH curves of the different ferromagnetic materials are compared in figure 21.

The machines were prototyped in a fast manner, thus, the manufacturing tolerances were not controlled. Despite the difference in the materials, the results show the same trends that were expected from the simulations. Figure 22 shows the C1 and C3 prototypes.

The tests were performed in the static test bench from figure 23. The Interface SMA-60N load cell was used to measure the static force, and the position was measured with an Omron ZX2-LD100L laser position sensor.

In total, the force was measured in 25 position points for each of the current values of the test. First, the primary of the machine was displaced to the measurement point, and then, the corresponding current steps were applied to the armature winding. The phase current references were calculated with a $i_d = 0$ control, and they were transmitted to the DC power supplies as current value set-points.

The main drawback of the setup in figure 23 is the presence of the static friction. The linear guides were carefully aligned with comparator gauges to minimise the influence of the friction. In order to account for the static friction, the no-load force was measured in the first place. The offset of the

This article has been accepted for publication in IEEE Transactions on Energy Conversion. This is the author's version which has not been fully edited and content may change prior to final publication. Citation information: DOI 10.1109/TEC.2022.3160505

IEEE TRANSACTIONS ON ENERGY CONVERSION, VOL. XX, NO. X, MONTH 20XX
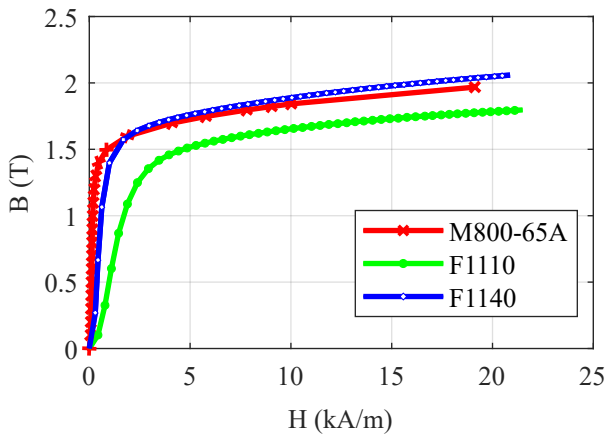8

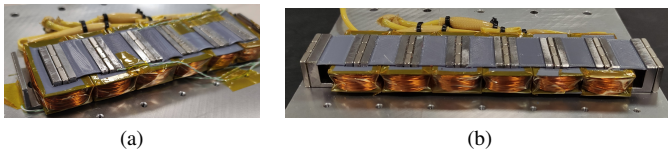Fig. 21: Comparison of the BH curves of the ferromagnetic materials.

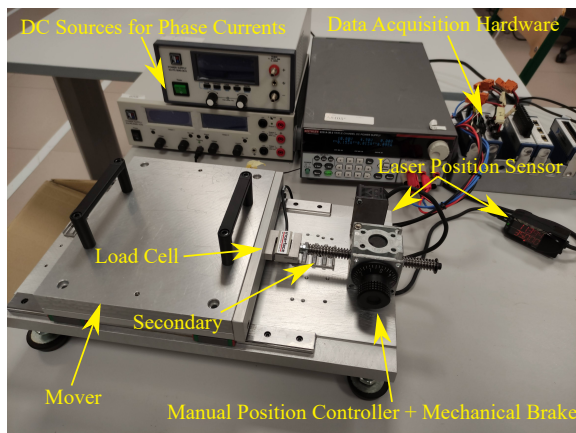Fig. 22: Prototyped machines. (a) C1 (b) C3.

Fig. 23: Static test bench.

no-load force corresponds to the static friction of the system. This value was then used to correct the measurements of the on-load test.

It can clearly be seen in figure 24 (a) that it is C3 which presents the lowest thrust ripple along the whole range of measurements. The measured peak to peak detent forces were 4.15 N for the initial machine, 3.71 N for C1, 28.42 N for C2, and 3.34 N for C3. The increase in the detent force of C2 is such, that this configuration is unable to reduce the original ripple at any point.

On the other hand, the average thrust force capability comparison from figure 24 (b) shows that the addition of extra PMs can even enhance the thrust capability of the machines. Thus, they are a very interesting alternative when optimising the performance of LSFPMs.

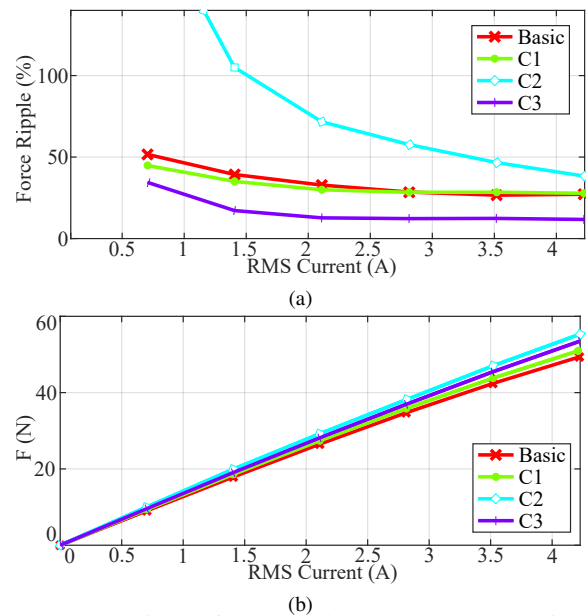In order to evaluate the level of precision of the 2D

Fig. 24: Comparison of measured results. (a) Thrust ripple vs RMS current, (b) Average thrust force vs RMS current.

simulations, the measured results and the values that were obtained in both 2D simulations and 3D simulations are compared in figure 25. Obviously, the experimental results are affected by several factors, such as manufacturing tolerances, measurement uncertainty etc. Hence, they do not coincide perfectly with any of the predictions. However, both the 2D and 3D FEM predictions can be considered accurate enough.

Finally, the optimisation studies were repeated with the solid materials for ensuring that the new materials would not influence the dimensions of the optimised ends of the machine in excess.

Table VI shows a summary of the results that were obtained in this optimisation. The table shows that because of the difference in the materials, the optimal values of the detent-force and the thrust ripple varied with respect to those which were shown in table V. Due to the lower relative permeability of the experimental materials, the back-EMF amplitude and the values of the optimised inductances with these materials were reduced.

Nonetheless, the optimal dimensions of the additional poles of the machine were the same as in table V for the configurations that were sized via a grid search. In the case of the GA based configurations, the values of the optimisation variables did vary with respect to table V. These differences can be attributed to the differences of the characteristics of the magnetic materials, and the stochastic nature of the search algorithm itself. Despite the differences, the new values can be considered to be close enough to the dimensions of the prototypes for the measurements to be representative of the performance of the optimised configurations.

Interestingly, the thrust ripple performance of the newly optimised machines was similar to the one that was obtained with the initial material, which suggests that from the viewpoint of the thrust ripple, there may not be a large benefit when adopting costly materials.

This article has been accepted for publication in IEEE Transactions on Energy Conversion. This is the author's version which has not been fully edited and content may change prior to final publication. Citation information: DOI 10.1109/TEC.2022.3160505

IEEE TRANSACTIONS ON ENERGY CONVERSION, VOL. XX, NO. X, MONTH 20XX 9
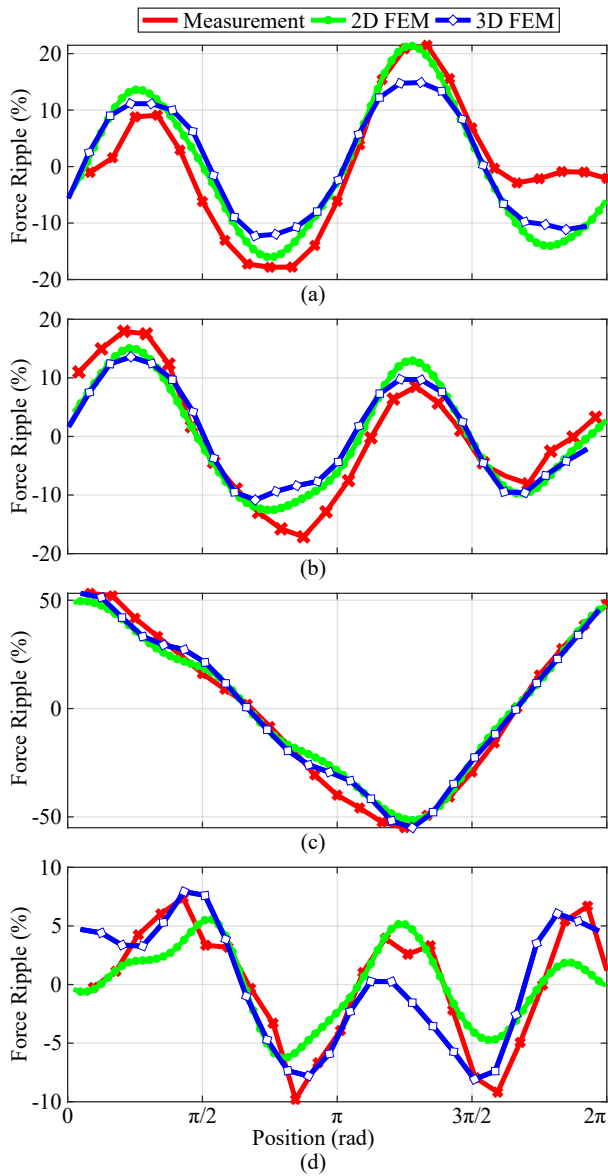

Fig. 25: Thrust ripple at rated load. (a) Initial, (b) passive assistant teeth, (c) C2, and (d) C3.

TABLE VI: Optimisation results for the solid materials. The optimisation variables are denoted with an asterisk (*).

Parameter	Initial	Passive Poles	Active Poles		
Objective	-	$F_d \downarrow, F_r \downarrow$	$E_a = E_b = E_c$	$F_d \downarrow$	$F_d \downarrow$ and $F_r \downarrow$
Method	-	GA	Grid search	Grid search	GA
ω_{let} (mm)	-	1.9*	4.1	5.5*	5.2*
ω_{ret} (mm)	-	5.40*	4.1	5.5*	4.45*
ω_{les} (mm)	6.4	12.85*	12.8	12.8	12.8
ω_{res} (mm)	6.4	10.10*	12.8	12.8	12.8
ω_{lepm} (mm)	-	-	5*	3	2.6*
ω_{repm} (mm)	-	-	5*	3	1.5*
F_d (N)	4.62	2.50	22.56	2.27	1.4
F_r (%)	36.17	25.86	96.78	11.06	9.43
E_a (V peak)	6.28	6.55	7.44	6.96	7.00
E_b (V peak)	7.52	7.83	7.44	7.76	7.74
E_c (V peak)	6.28	6.55	7.44	6.96	6.96
L_{aa} (mH)	4.50	5.02	5.11	5.17	5.16
L_{bb} (mH)	5.14	5.19	5.22	5.23	5.21
L_{cc} (mH)	4.50	5.17	5.11	5.17	5.13
M_{ab} (mH)	-2.29	-2.15	-2.12	-2.11	-2.11
M_{bc} (mH)	-2.29	-2.11	-2.12	-2.11	-2.11
M_{ca} (mH)	-1.53	-1.43	-1.43	-1.42	-1.42

VI. CONCLUSIONS

In this article, the optimal additional pole configuration was discussed for the reduction of the thrust ripple of linear switched-flux PM machines. The 2D FEM results showed that the 2 new design solutions presented in this paper have a superior performance when minimising both the detent force and the rated thrust ripple. The experimental comparison of one of the new solutions with the previously existing configurations also demonstrated that the new solution is much more effective when minimising the thrust fluctuations. Moreover, the experimental results showed that the new solution can reduce the thrust ripple with high efficacy over a wide supply current range.

Using a single size of PMs in the whole machine, including the PMs of the additional poles, and minimising the peak to peak detent force via the widths of the additional teeth was found to be a very simple and effective way to minimise the thrust ripples. This configuration was previously not explored in the literature. It can be concluded that when the cost of the additional PMs is allowed, this should be the generic alternative when dealing with the thrust ripples. This strategy combines the simplicity and ease of design of the passive additional poles with the high effectiveness of the active additional poles.

The genetic algorithm based strategy was also found to be very effective, especially for the no-load detent force. However, the final design is required to have more individual parts, and thus, it would also increase the manufacturing complexity and cost of the final design.

It was also confirmed that none of these configurations are able to suppress the unbalance between the electrical parameters of the machine. Hence, conventional PI based control systems could find it difficult to produce purely sinusoidal currents. This, in turn, would increase the thrust ripple. In this aspect, hysteresis controllers should be able to ensure the supply of sinusoidal currents to these machines [23]. Thus, the usage of such controllers should be considered when adopting one of these configurations.

The optimisation with the solid materials also showed an interesting result. The detent force and the on load thrust ripple of some configurations were similar with the carbon steel when compared to those which were obtained with the higher permeability silicon steel. This is an interesting finding, because it means that some applications, e. g. high precision machine tooling, where the requirements for the machine are very focused on its ripple performance, could benefit from the usage of lower permeability magnetic materials for a reduced manufacturing cost of the machines, if there is margin for a lowered efficiency.

The article demonstrated that existing linear machines could benefit from modifying the assistant ends of the mover to minimise the thrust ripple. A global optimisation including the design variables of the active part of the machine could also improve the performance of the proposed configurations, but the improvement would not be as significant. Hence, the proposed configurations are very interesting from the industrial
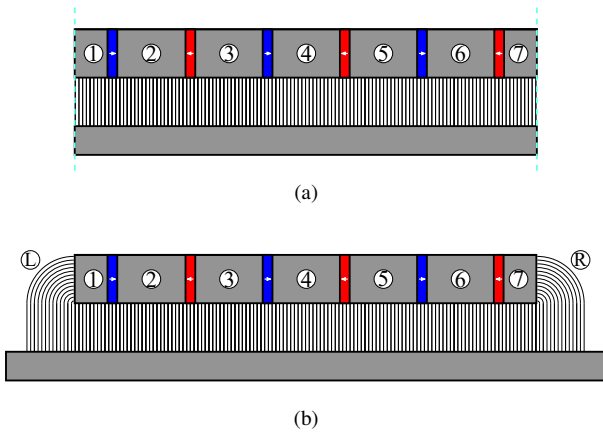
(a)

(b)

Fig. 26: Simplified models for the derivation of the end Carter coefficient. (a) Ideal, and (b) single module with end-effect.

viewpoint, due to the need of a low magnitude of investment and a high reward in performance.

Further work from the authors will focus on the modelling and the enhancement of the thrust density and power factor of switched-flux machines.

APPENDIX
DERIVATION OF THE CARTER COEFFICIENT

In this simplified example, a single-module, periodic and slot-less machine is defined first for the analysis of the ideal case. Figure 26 (a) shows the flux lines of this model. Notice that the flux is enclosed inside the active part of the machine in this model. Hence, the end-effect is avoided in this ideal scenario.

Assuming that the magnets introduce a square-wave magneto-motive force, F_p, into the circuit, it can be assumed that the magnitude of the flux of the cores can be obtained following

$$|\phi_1| = |\phi_7| = \mu_0 \frac{F_p l_{stk}}{g} 0.5\tau_p, \text{ and} \tag{4}$$

$$|\phi_2| = |\phi_3| = |\phi_4| = |\phi_5| = |\phi_6| = \mu_0 \frac{F_p l_{stk}}{g} \tau_p. \tag{5}$$

Hence, the totalised equivalent flux of the mahcine, ϕ_t, which results from the sum of the flux of the cores is

$$\phi_t = 6\mu_0 \frac{F_p l_{stk}}{g} \tau_p. \tag{6}$$

In a machine that is affected by the end-effect, and assuming that the flux that is introduced by the magnets in the magnetic circuit stays constant, the flux in the airgap regions below the leading and trailing ends of the machine is reduced. Hence, the magneto-motive force is also decreased in those airgap regions.

The new flux of regions 1 and 7, ϕ_{1e} and ϕ_{7e} must therefore be obtained from the new value of the magneto-motive force, F_e,

$$|\phi_{1e}| = |\phi_{7e}| = \mu_0 \frac{F_e l_{stk}}{g} 0.5\tau_p. \tag{7}$$

Assuming a semicircular path of the magnetic flux in the ends of the machine as shown in figure 26, the airgap length of the flux line at radius x, g_x can be defined as

$$g_x = g + \frac{\pi}{2}x, \tag{8}$$

and the field intensity along the path, H_x, as

$$H_x = \frac{F_e}{g_x} = \frac{F_e}{g + \frac{\pi}{2}x}. \tag{9}$$

The magnitude of the flux that leaks towards the left and right ends of the machine, $|\phi_L|$ and $|\phi_R|$, can now be obtained from

$$|\phi_L| = |\phi_R| = \int_0^{\omega_e} \mu_0 H_x l_{stk} dx, \tag{10}$$

which after some operation becomes

$$|\phi_L| = |\phi_R| = \frac{2\mu_0 l_{stk} F_e}{\pi} \ln\left(1 + \frac{\pi \omega_e}{2g}\right), \tag{11}$$

where ω_e is the width of the end of the machine. Notice that the limit of (11) as $\omega_e \to \infty$ equals to ∞. Hence, the value of ω_e must be restricted for the expression to be valid. In this case, the height of the primary of the machine was used to approximate the value of ω_e.

As we know that

$$|\phi_1| + |\phi_7| = |\phi_{1e}| + |\phi_{7e}| + |\phi_L| + |\phi_R|, \tag{12}$$

it can be deduced that the new value of the magneto-motive force in the leading and the trailing ends of the machine is

$$F_e = \frac{F_p \tau_p}{\tau_p + \frac{4g}{\pi} \ln\left(1 + \frac{\pi \omega_e}{2g}\right)}. \tag{13}$$

Now, the new value of the airgap flux below regions 1 and 7 can be obtained from

$$|\phi_{1e}| = |\phi_{7e}| = \mu_0 \frac{l_{stk} F_p \tau_p}{g\left(\tau_p + \frac{4g}{\pi} \ln\left(1 + \frac{\pi \omega_e}{2g}\right)\right)} 0.5\tau_p, \tag{14}$$

and the totalised equivalent magnitude of the flux, accounting for the end-effect, $|\phi_{te}|$, is

$$|\phi_{te}| = 5\mu_0 \frac{F_p l_{stk}}{g} \tau_p + \mu_0 \frac{l_{stk} F_p \tau_p}{g\left(\tau_p + \frac{4g}{\pi} \ln\left(1 + \frac{\pi \omega_e}{2g}\right)\right)} \tau_p. \tag{15}$$

Finally, the value of the Carter coefficient, K_c, to account for the end effect is obtained from the division between the ideal flux and the real flux

$$K_c = \frac{6}{5 + \frac{1}{1 + \frac{4g}{\pi \tau_p} \ln\left(1 + \frac{\pi \omega_e}{2g}\right)}}. \tag{16}$$

REFERENCES

[1] I. Eguren, G. Almandoz, A. Egea, G. Ugalde, and A. J. Escalada, "Linear Machines for Long Stroke Applications—A Review," *IEEE Access*, vol. 8, pp. 3960–3979, 2020.

[2] R. Cao, M. Lu, N. Jiang, and M. Cheng, "Comparison Between Linear Induction Motor and Linear Flux-switching Permanent-Magnet Motor for Railway Transportation," *IEEE Transactions on Industrial Electronics*, vol. PP, no. c, p. 1, 2019.

[3] X. zhen Huang, H. C. Yu, B. Zhou, L. Y. Li, D. Gerada, C. Gerada, and Z. Y. Qian, "Detent-Force Minimization of Double-Sided Permanent Magnet Linear Synchronous Motor by Shifting One of the Primary Components," *IEEE Transactions on Industrial Electronics*, vol. 67, no. 1, pp. 180–191, 2020.

[4] D. Wang, D. Zhang, X. Du, and X. Wang, "Unitized Design Methodology of Linear Switched Reluctance Motor With Segmental Secondary for Long Rail Propulsion Application," *IEEE Transactions on Industrial Electronics*, vol. 65, no. 12, pp. 9884–9894, 2018.

[5] W. Hao and Y. Wang, "Thrust Force Ripple Reduction of Two C-Core Linear Flux-Switching Permanent Magnet Machines of High Thrust Force Capability," *Energies*, vol. 10, no. 10, p. 1608, 2017.

[6] D. Dong, W. Huang, F. Bu, Q. Wang, W. Jiang, and X. Lin, "Modeling and Static Analysis of Primary Consequent-Pole Tubular Transverse-Flux Flux-Reversal Linear Machine," *Energies*, vol. 10, no. 10, p. 1479, 2017.

[7] R. Cao, Y. Jin, Z. Zhang, and M. Cheng, "A New Double-Sided Linear Flux Switching Permanent Magnet Motor with Yokeless Mover for Electromagnetic Launch System," *IEEE Transactions on Energy Conversion*, vol. PP, no. 51877109, p. 1, 2018.

[8] W. Hao and Y. Wang, "Analysis of double-sided sandwiched linear flux-switching permanent-magnet machines with staggered stator teeth for urban rail transit," *IET Electrical Systems in Transportation*, vol. 8, no. 3, pp. 175–181, 2018.

[9] Z. Q. Zhu, "Switched flux permanent magnet machines - Innovation continues," *2011 International Conference on Electrical Machines and Systems, ICEMS 2011*, no. c, 2011.

[10] A. L. Shuraiji, Z. Q. Zhu, and Q. F. Lu, "A Novel Partitioned Stator Flux Reversal Permanent Magnet Linear Machine," *IEEE Transactions on Magnetics*, vol. 52, no. 1, pp. 1–6, 2016.

[11] Q. Tan, X. Huang, L. Li, and M. Wang, "Research on Inductance Unbalance and Thrust Ripple Suppression of Slot-Less Tubular Permanent Magnet Synchronous Linear Motor," *IEEE Access*, vol. 6, pp. 51 011–51 020, 2018.

[12] M. Inoue and K. Sato, "An approach to a suitable stator length for minimizing the detent force of permanent magnet linear synchronous motors," *IEEE Transactions on Magnetics*, vol. 36, no. 4, pp. 1890–1893, jul 2000.

[13] J. Wang, M. Inoue, Y. Amara, and D. Howe, "Cogging-force-reduction techniques for linear permanent-magnet machines," *IEE Proceedings - Electric Power Applications*, vol. 152, no. 3, p. 731, 2005.

[14] W. Min, J. T. Chen, Z. Q. Zhu, Y. Zhu, M. Zhang, and G. H. Duan, "Optimization and Comparison of Novel E-Core and C-Core Linear Switched Flux PM Machines," *IEEE Transactions on Magnetics*, vol. 47, no. 8, pp. 2134–2141, 2011.

[15] C. F. Wang, J. X. Shen, Y. Wang, L. L. Wang, and M. J. Jin, "A new method for reduction of detent force in permanent magnet flux-switching linear motors," *IEEE Transactions on Magnetics*, vol. 45, no. 6, pp. 2843–2846, 2009.

[16] F. Xiao, X. Liu, Y. Du, K. Shi, and P. Xu, "A C-core linear flux-switching permanent magnet machine with positive additional teeth," in *2014 17th International Conference on Electrical Machines and Systems (ICEMS)*. IEEE, oct 2014, pp. 1757–1761.

[17] Y. Du, G. Yang, L. Quan, X. Zhu, F. Xiao, and H. Wu, "Detent force reduction of a C-core linear flux-switching permanent magnet machine with multiple additional teeth," *Energies*, vol. 10, no. 3, 2017.

[18] R. Cao, M. Cheng, and W. Hua, "Investigation and General Design Principle of a New Series of Complementary and Modular Linear FSPM Motors," *IEEE Transactions on Industrial Electronics*, vol. 60, no. 12, pp. 5436–5446, 2013.

[19] R. Cao, M. Cheng, C. Mi, W. Hua, X. Wang, and W. Zhao, "Modeling of a Complementary and Modular Linear Flux-Switching Permanent Magnet Motor for Urban Rail Transit Applications," *IEEE Transactions on Energy Conversion*, vol. 27, no. 2, pp. 489–497, 2012.

[20] I. Eguren, G. Almandoz, A. Egea, S. Zarate, and A. Urdangarin, "End Magnet Optimisation for the Reduction of the Thrust Ripple of Linear Switched-Flux Machines," in *2020 International Conference on Electrical Machines (ICEM)*. IEEE, aug 2020, pp. 700–706.

[21] Q. Lu, Y. Li, Y. Ye, J. T. Chen, and Z. Q. Zhu, "Novel linear switched-flux PM machine with 9/10 primary/secondary pole number combination," *COMPEL - The international journal for computation and mathematics in electrical and electronic engineering*, vol. 34, no. 6, pp. 1656–1672, 2015.

[22] K. Deb, A. Pratap, S. Agarwal, and T. Meyarivan, "A fast and elitist multiobjective genetic algorithm: NSGA-II," *IEEE Transactions on Evolutionary Computation*, vol. 6, no. 2, pp. 182–197, 2002.

[23] B. Bose, "An adaptive hysteresis-band current control technique of a voltage-fed PWM inverter for machine drive system," *IEEE Transactions on Industrial Electronics*, vol. 37, no. 5, pp. 402–408, 1990.

Imanol Eguren was born in Anoeta, Basque Country, Spain, in 1993. He received the B.S. degree in electronics engineering from Mondragon Unibertsitatea, Arrasate, Spain, in 2015, where he is currently pursuing the Ph.D. degree.

His current research interest includes design, control, and optimisation of linear machines.

Gaizka Almandoz (M'04) was born in Arantza, Spain. He received the B.Sc. and Ph.D. degrees in electrical engineering from Mondragon Unibertsitatea, Mondragon, Spain, in 2003 and 2008, respectively.

Since 2003, he has been with the Electronics and Computing Department, Faculty of Engineering, Mondragon Unibertsitatea, where he is currently an Associate Professor. His current research interest includes electrical machine design, modeling, and control. He has participated in various research projects in the fields of wind energy systems, elevator drive, and railway traction.

Aritz Egea received the degree in electrical engineering from the University of Mondragon, Mondragon, Spain, in 2009, and the Ph.D. degree in electrical engineering, in 2012.

He is currently an Associate Professor with the Faculty of Engineering, Mondragon Unibertsitatea. His current research interests include electrical machine design and control and electromagnetic actuators.

Sergio Zarate was born in Vitoria-Gasteiz, Spain. He received the B.Sc., M.Sc. and Ph.D. degrees in electrical engineering at Mondragon Unibertsitatea, Mondragon, Spain, in 2012, 2014 and 2018, respectively.

Since 2018, he has been with the Electronics department of the Faculty of Engineering of Mondragon Unibertsitatea, where he is currently a Lecturer and Researcher. His current research interests include drives, electrical machines vibration and permanent magnet machine design and optimization.

Ander Urdangarin was born in Ordizia, Spain, in February 1982. He received the B.S. degree in Automatic and industrial electronics from Mondragon Unibertsitatea, Mondragón, Spain in 2009. Between 2010-2012 he was with the Department of Electronics, Faculty of Engineering of Mondragon Unibertsitatea.

Since 2012 he is member of ORONA. His current research interests include power electronics design, modelling, and control.